BEAMLINE MAP COMPUTATION FOR PARAXIAL OPTICS

B. Nash*, N. Goldring, J. P. Edelen, S. Webb
RadiaSoft LLC, Boulder, CO, USA

Abstract

Modeling of radiation transport is an important topic tightly coupled to many charged particle dynamics simulations for synchrotron light sources and FEL facilities. The radiation results from the electron dynamics and then passes through beamlines, either directly to an experiment or may be recirculated back to interact with the electron beam in the case of an FEL oscillator. The Wigner function representation of these wavefronts have been described in the literature, and is the closest relation to the phase space description of charged particle dynamics. We describe this formalism and the computation of phase space maps using the code SRW, applying this to the case of a 4 crystal FELO 1:1 imaging beamline, resulting in a substantial speed-up in computation time.

INTRODUCTION

Optical beamlines for radiation transport are crucial components of many scientific facilities. They may be used to transport radiation from the electron beam source in a synchrotron light source, or in recirculation optics in a free electron laser oscillator (FELO) to improve longitudinal coherence of the radiation. Numerous codes exist to model the radiation transport through the beamline elements typically either using a ray tracing, geometrical optics approach (e.g. SHADOW [1]), or a physical optics wavefront propagation approach (e.g. SRW [2]). The wavefront propagation captures more of the optical physics, but can be highly intensive computationally.

For FELO and synchrotron light source modeling, one requires many passes of radiation through a beamline, while varying either the initial conditions, or some beamline parameters. A more compact representation of a beamline is desired for such calculations.

In this paper, we consider a map based approach to beamline modeling that, once computed, allows a large range of initial conditions to be rapidly transported through the beamline. The formalism we use for representing the wavefront is based on the Wigner function, pioneered in x-ray optics by K. J. Kim [3]. Although the general non-linear map applied to the Wigner function may be quite complex, in the case of linear transport (so-called ABCD matrix, in the optics literature), the transformation is quite straight forward.

We provide a proof of principle for this method, applied to an FELO recirculation optics beamline, with radiation transport of increasing complexity. The beamline is shown in Fig. 1. The radiation transport starts at the end of the undulator and diffracts off the crystals in Bragg geometry. A single ideal lens is used for focussing the radiation back

_____
* bnash@radiasoft.net

to the beginning of the undulator for the next pass. We first consider Gaussian wavefronts, in which case, only transport of second moments is necessary. We set up the beamline in SRW and propagate the initial wavefront. We also compute the transfer matrix for the beamline to transport the Wigner function. For the Gaussian case, only the moments need be transported, but we also apply the method to the numerical Gaussian to check our calculation of the Wigner function. Finally, we consider a non-Gaussian case of an $m_x = 2$ Hermite Gaussian mode, to show the generality of the method. In each case, we compare the SRW simulation to the linear transport of the Wigner function, to confirm that the method is sound. One important difference between our Wigner function transport and the wavefront propagation, is the absorption effect in the crystals. However, since ideal crystals don't affect the wavefront distribution, only the intensity, the two effects can be treated separately.

Figure 1: Four crystal FELO beamline schematic as described in reference [4].

LINEAR PARAXIAL OPTICS PROPAGATION

We start by briefly reviewing the evolution equations for a wavefront with wavelength λ propagating through empty space. By this means we will set our notation, and clarify the issue of separability, which we will be assuming. We consider one component of an electric field travelling in the z direction, which we write as

$$E(x, y, z; t) = \bar{E}(x, y, z)e^{i(kz-\omega t)}, \qquad (1)$$

where $k = \frac{2\pi}{\lambda}$ and $\omega = ck$. The paraxial Helmholtz equation for the evolution of the electric field in free space is given by

$$\nabla_{\perp}^2 E + 2ik\frac{\partial E}{\partial z} = 0, \qquad (2)$$

where

$$\nabla_{\perp}^2 = \frac{\partial^2}{\partial x^2} + \frac{\partial^2}{\partial y^2} \qquad (3)$$

and we have assumed

$$\frac{\partial^2 \bar{E}}{\partial z^2} \ll 2ik\frac{\partial \bar{E}}{\partial z} \qquad (4)$$

(i.e. a slow change in transverse envelope relative to the wavelength). Equation (2) may be solved to yield Fresnel propagation of the electric field. In this paper, we will assume electric fields which satisfy the separability condition

$$E(x, y; z) = E_0 E_x(x; z)E_y(y; z), \qquad (5)$$

where E_0 is a constant with units of electric field.

For the case of separable electric fields, Fresnel propagation may be written in the following form.

$$E(x, y; z + l) = E_0 e^{i(kl-\frac{\pi}{2})} E_x(x; z + l)E_y(y; z + l), \quad (6)$$

where

$$E_x(x; z + l) = \frac{1}{\sqrt{\lambda l}} \int_{-\infty}^{\infty} E_x(x'; z)e^{\frac{ik}{2l}(x-x')^2} dx' \qquad (7)$$

and likewise for E_y.

The angular representation $E(\theta)$ for either component is given by

$$E(\theta) = \frac{1}{\sqrt{\lambda}} \int_{-\infty}^{\infty} E(x)e^{-\frac{2\pi i}{\lambda}\theta x} dx. \qquad (8)$$

In this representation, the propagation is simply given by

$$E(\theta; z + l) = E(\theta; z)e^{\frac{2\pi i l}{\lambda}\left(1-\frac{\theta^2}{2}\right)}. \qquad (9)$$

We normalize the separate field components such that[1]

$$\int_{-\infty}^{\infty} E^*(x)E(x)dx = 1, \qquad (10)$$

$$\int_{-\infty}^{\infty} E^*(\theta)E(\theta)d\theta = 1. \qquad (11)$$

The second moments of the field distribution in coordinate and angular representations may now be calculated as

$$< x^2 > \quad = \quad \int_{-\infty}^{\infty} x^2 E^*(x)E(x)dx, \qquad (12)$$

$$< \theta^2 > \quad = \quad \int_{-\infty}^{\infty} \theta^2 E^*(\theta)E(\theta)d\theta. \qquad (13)$$

We now introduce the Wigner function defined from the electric field, $E(x)$, as follows

$$W(x, \theta) = \frac{1}{\lambda} \int_{-\infty}^{\infty} E^*(x - \frac{\phi}{2})E(x + \frac{\phi}{2})e^{\frac{-2\pi i}{\lambda}\phi\theta} d\phi, \quad (14)$$

---

[1] Note that we have normalized the electric field in the same way as wave functions are normalized in quantum mechanics. In fact, much of the formalism of quantum mechanics may now be directly applied with the proviso that Planck's constant, $\hbar$, be replaced by the reduced wavelength $\lambda = \lambda/2\pi$.

where $W(x, \theta)$ will be normalized as

$$\int_{-\infty}^{\infty} \int_{-\infty}^{\infty} W(x, \theta)dxd\theta = 1. \qquad (15)$$

The Wigner function can be thought of as a probability distribution in phase space except for the fact that it may become negative. The second moments are given simply as

$$< x^2 > \quad = \quad \int_{-\infty}^{\infty} \int_{-\infty}^{\infty} x^2 W(x, \theta)dxd\theta, \qquad (16)$$

$$< \theta^2 > \quad = \quad \int_{-\infty}^{\infty} \int_{-\infty}^{\infty} \theta^2 W(x, \theta)dxd\theta, \qquad (17)$$

$$< x\theta > \quad = \quad \int_{-\infty}^{\infty} \int_{-\infty}^{\infty} x\theta W(x, \theta)dxd\theta. \qquad (18)$$

For propagation of the Wigner function, we briefly give a general formulation before reducing to the simplified linear case. To do so, we assume the existence of a Hamiltonian, $H(x, \theta; z)$. We assume that we stay within the paraxial approximation, and ignore the effect of absorption. The evolution equation for the Wigner function is then given as follows [5]

$$\frac{\partial W(x, \theta; z)}{\partial z} = [W, H]_*, \qquad (19)$$

where the Moyal bracket is defined for arbitrary phase space functions f and g as

$$[f, g]_* = \frac{1}{i\lambda}(f * g - g * f) \qquad (20)$$

and the Moyal star is given by

$$* = e^{\frac{i\lambda}{2}\left(\overleftarrow{\partial}_x \overrightarrow{\partial}_\theta - \overleftarrow{\partial}_\theta \overrightarrow{\partial}_x\right)} \qquad (21)$$

with the arrows representing action of the derivative, either to the left or right, depending on arrow orientation.

Fortunately, in the case of a quadratic Hamiltonian, evolution of the Wigner function is much more simple and intuitive. Only first order in λ is needed, and the Moyal bracket reduces to the Poisson bracket giving classical evolution (again using the quantum/classical mechanics analogy). One finds that the motion in phase space is a linear transformation. These considerations allow us to formulate our approach. In particular, consider a paraxial beamline where the geometric optics will be defined by a transfer matrix M acting on the phase space vector $\vec{z}$:

$$\vec{z}_f = M\vec{z}_i, \qquad \vec{z} = \begin{pmatrix} x \\ \theta \end{pmatrix}. \qquad (22)$$

The Wigner function will evolve along this beamline according to

$$W_f(\vec{z}) = W_i(M\vec{z}). \qquad (23)$$

The electric field may be reconstructed from the Wigner function as follows [6]

$$E^*(x)E(0) = \frac{1}{\lambda} \int_{-\infty}^{\infty} W\left(\frac{x}{2}, \theta\right) e^{\frac{2\pi i}{\lambda}x\theta} d\theta. \qquad (24)$$

Hermite Gaussian Modes

The Hermite Gaussian modes will satisfy the separability condition (5). These modes are defined by

$$E_m(x) = E_{0,m} H_m\left(\frac{\sqrt{2}x}{w(z)}\right) e^{-i\frac{kx^2}{2q(z)}}, \qquad (25)$$

where $E_{0,m}$ is the normalization factor resulting in the normalization condition (10) [7]. $q(z)$ is the complex beam parameter defined in terms of the beam radius of curvature, $R(z)$, and beam spot size, $w(z)$:

$$\frac{1}{q(z)} \equiv \frac{1}{R(z)} - i\frac{\lambda}{\pi w^2(z)}. \qquad (26)$$

In empty space the beam spot size evolves as

$$w(z) = w_0\sqrt{1 - \left(\frac{z}{z_R}\right)^2} \qquad (27)$$

with z_R the Raleigh length, given by

$$z_R = \frac{\pi w_0^2}{\lambda}, \qquad (28)$$

and w_0 is the beam spot size at waist. The radius of curvature $R(z)$ evolves as

$$R(z) = z\left[1 + \left(\frac{z_R}{z}\right)^2\right]. \qquad (29)$$

For the case $m = 0$, we have a Gaussian field given explicitly by

$$E(x) = \frac{1}{(2\pi\sigma_x^2)^{1/4}} e^{-\frac{x^2}{4\sigma_x^2}}, \qquad (30)$$

where σ_x is the RMS size of the distribution. One can relate σ_x to the beam spot size at waist via the equation $w_0 = 2\sigma_x$. This Gaussian distribution will satisfy the diffraction limit which implies the following relation between the RMS size and divergence

$$\sigma_x\sigma_\theta = \frac{\lambda}{4\pi}. \qquad (31)$$

For the Gaussian case, the Wigner function propagation may be reduced to a transformation of the second moments. In particular, under a transfer matrix M, the second moments will evolve as follows:

$$\Sigma_f = M\Sigma_i M^T, \qquad (32)$$

where the second moment matrix is given by

$$\Sigma = \begin{pmatrix} \langle x^2 \rangle & \langle x\theta \rangle \\ \langle x\theta \rangle & \langle \theta^2 \rangle \end{pmatrix}. \qquad (33)$$

MOMENT CALCULATIONS FOR FELO BEAMLINE AND COMPARISON WITH SRW

We have set up the four crystal beamline as described in reference [4]. Note however that we've used even simpler optics, with just a single ideal lens, located at the midpoint of the beamline. See Fig. 1 for the schematic. The parameters used for this example calculation are as follows. The undulator length, L_u is 10 meters. The total length, L, is 100 meters. The crystal diffraction angle, θ, is $\pi/8$. The length of the lower leg of the beamline, S, is 3 meters. The other parameters are then determined by geometric relations and are as follows. L_1 and L_6 are 45.0 meters. L_2 and L_5 are 72.8 meters. L_3 and L_4 are 1.5 meters. The distance between the two legs of the beamline, G, is 51.5 meters.

The reflecting crystals were chosen to be diamond with a d-spacing of 0.892 Å. The crystal thickness was 10 millimeters. The real and imaginary parts of the 0-th Fourier component of crystal polarizability were -0.217×10^{-4} and 0.280×10^{-7} respectively. The real and imaginary parts of the next Fourier component of crystal polarizability was -0.544×10^{-5} and 0.259×10^{-7} respectively.

In order to compare to the analytical approach, we need to compute the transfer matrix M for the beamline. The effect of the crystal is only to decrease the electric field amplitude, and not change the wavefront distribution. Thus, disregarding this absorption effect, we may ignore the crystals in our analytical calculation. The transfer matrix may be calculated using the matrices for a drift, M_d, and for an ideal lens, M_f. These are given by

$$M_d = \begin{pmatrix} 1 & l \\ 0 & 1 \end{pmatrix}, \qquad (34)$$

$$M_f = \begin{pmatrix} 1 & 0 \\ -\frac{1}{f} & 1 \end{pmatrix}, \qquad (35)$$

where l is the drift length and f is the focal length for the ideal lens. The total transfer matrix M_T is then given by multiplying the component matrices for the beamline. The transfer matrix for the simple single lens beamline is given by

$$M_T = M_d M_f M_d \qquad (36)$$

$$= \begin{pmatrix} 1 - \frac{l}{f} & 2l - \frac{l^2}{f} \\ -\frac{1}{f} & 1 - \frac{l}{f} \end{pmatrix}. \qquad (37)$$

In the case that $f = l/2$ the transfer matrix simplifies to

$$M_T = \begin{pmatrix} -1 & 0 \\ -\frac{2}{l} & -1 \end{pmatrix}. \qquad (38)$$

To look at the effect of focusing errors, we have allowed the focal length to vary from the nominal value by defining $f = \frac{l}{2}(1 + \frac{df}{f})$. For varying values of $\frac{df}{f}$, we have set up a computation in SRW and also compared it to this moment

calculation. The results are shown in Fig. 2. The SRW calculation is a wavefront calculation. In order to compute the divergence, we convert the wavefront to angular coordinates, and then compute the RMS of the distribution. The initial RMS beamsize for the Gaussian chosen was 10 micrometers. Applying Eq. (31), we find an initial divergence at the waist of 0.987 microradians.

We now give more details for the SRW simulation. The initial Gaussian wavefront was represented on a grid of size 42×42. Each beamline element requires specification of propagation parameters. These were chosen for drift, crystal, and lens elements to ensure accuracy and avoid excessive computational overhead. The final grid size needed to capture the full Gaussian ended up ranging from 42×42 to 52×52 as $\frac{df}{f}$ was varied.

SRW was run on the Radiasoft Jupyter server [8]. The time required for the full SRW calculation was 12.8 seconds and the time required for the matrix computation was 0.21 seconds. Note that the time for the SRW calculation includes the transformation of the wavefront from coordinate to angular representation (see Eq. (8)) in order to compute RMS divergences. The matrix transformation amounts to a speedup of a factor of 608 over the SRW calculation.
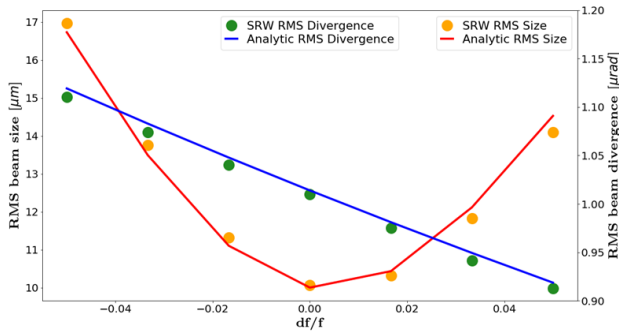
Figure 2: Comparison between RMS size and divergence as a function of focal length for the four crystal FELO beamline.

NUMERICAL WIGNER FUNCTION EVOLUTION AND SRW COMPARISON

In order to consider non-Gaussian wavefronts, we need to move beyond calculation of second moments. This requires numerical calculation of the Wigner function and inversion to reconstruct the electric field after propagation using Eq. (24). To demonstrate this procedure and explore the efficiency of the algorithms, we have implemented the Wigner function calculation and inversion formulae numerically. We first consider Gaussian distributions and then give results for an $m_x = 2$ Hermite Gaussian mode. The beams are assumed to start at a waist and are then propagated through the four crystal FELO recirculation beamline. Because of the separability condition for Hermite Gaussian modes, we can propagate the 2D wavefronts in SRW and compare the results between the map method and SRW for each individual component.

Gaussian Wigner Function

We now consider the results for Gaussian wavefronts. We start with a Gaussian wavefront at a waist with an RMS beam size of $10\,\mu$m. We consider x-rays of energy 10 keV which corresponds to a wavelength of 1.23 Å. For the diffraction limited Gaussians satisfying Eq. (31), the divergence is found to be 0.987 μrad. We construct such an initial Gaussian wavefront for input to SRW for propagation. We propagate the Gaussian through the FELO beamline we have described. The initial grid size was 2100×2100 and the grid size for the propagated wavefront was 3150×3150. The initial and final wavefront intensity distributions are shown in Fig. 3. Because of the one to one focusing optics, the initial and final intensity distributions are equal although the wavefronts themselves will differ. Due to the absorption from the crystals in the beamline, the final intensity computed with SRW is reduced from the initial intensity. We find a reflection coefficient of $R = 0.96$ where we define R as

$$R = \frac{\Phi_f}{\Phi_i} = \frac{\iint I_f(x,y)dxdy}{\iint I_i(x,y)dxdy}, \qquad (39)$$

i.e. Φ_i and Φ_f are the initial and final total fluxes of the distribution.
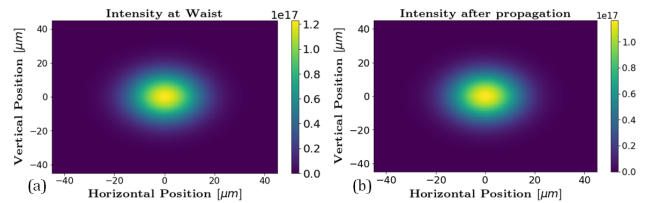
Figure 3: Gaussian intensity distribution at a) waist and b) after SRW propagation through FELO beamline.

In order to apply the map method, we have taken a horizontal slice of the initial electric field generated by SRW. We normalize this according to Eq. (10). We now compute the numerical Wigner distribution which will also be Gaussian. Next we apply the transfer matrix for the FELO recirculation optics, Eq. (38). The transformed Wigner function is then redeposited onto the initial grid. Initial transformed and redeposited Wigner functions are shown in Fig. 4. Note that for our angular variable, we have used $q = \theta/\lambda$.

Given the propagated Wigner function, we reconstruct the electric field using Eq. (24) and compare this to the results found from SRW. We see good agreement which is presented in Fig. 5.

(a) (b) (c)
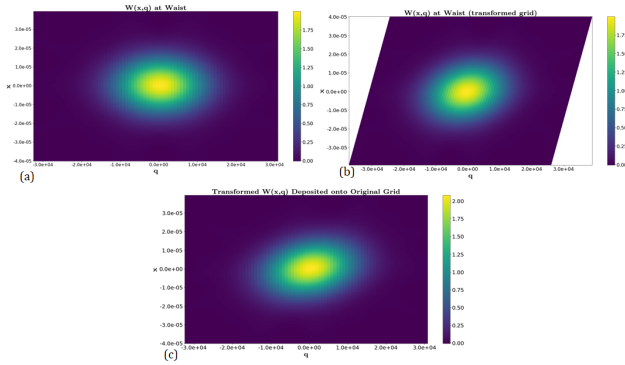
Figure 4: Numerically computed Wigner distributions a) at waist, b) after application of FELO beamline transfer matrix, and c) after redeposition of b) on initial grid.

(a) (b) (c)
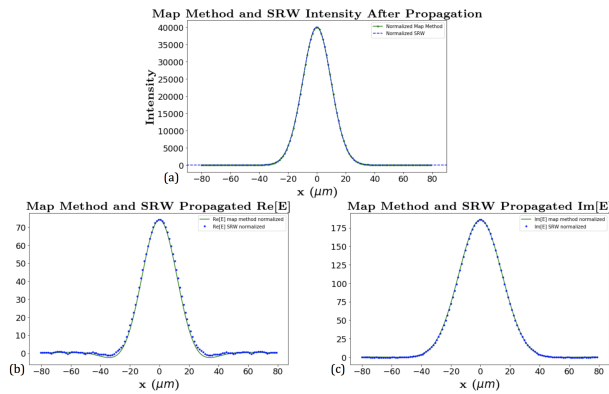
Figure 5: Comparison of SRW and map method propagation results for a) intensity, b) Re[E], and c) Im[E].

$m_x = 2$ Hermite Mode Wigner Function

We now present the results for an $m_x = 2$ Hermite Gaussian mode. As in the Gaussian case, we start at a waist and subsequently propagate the mode, using SRW, through the four crystal FELO beamline, using the same grid sizes as in the Gaussian case. We again consider x-rays of energy 10 keV, corresponding to a wavelength of 1.23 Å. Next, the exact same method as used in the Gaussian case was applied for the $m_x = 2$ mode. The Wigner function was computed and transformed with the transfer matrix and the distribution was redeposited onto the initial grid. This is shown in Fig. 7. Note in particular the large region in which the Wigner function takes on negative values outside the central peak. Finally, the electric field was again reconstructed using Eq. (24). Again, due to the one to one focusing beamline, the intensity distributions shown in Fig. 6 are equal whereas the electric field distributions shown in Fig. 8 are not and one can see the inversion from the transfer matrix in the field components. The final comparison between intensity and real and imaginary parts of the electric field for the two different methods are shown in Fig. 9. We see that the map method has agreed well with the SRW calculation.

(a) (b)
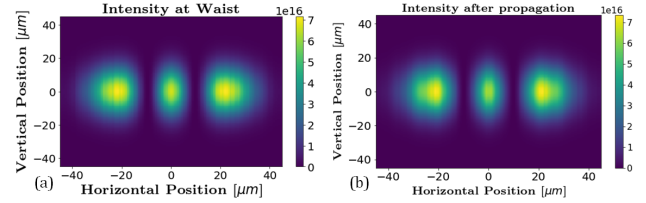
Figure 6: $m_x = 2$ Hermite mode intensity distribution at a) waist and b) after SRW propagation through FELO beamline.

(a) (b) (c)
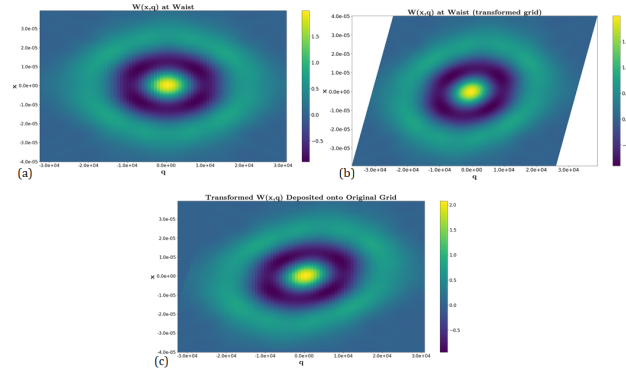
Figure 7: Numerically computed Wigner distributions a) at waist, b) after application of FELO beamline transfer matrix, and c) after redeposition of b) on initial grid.

(a) (b)
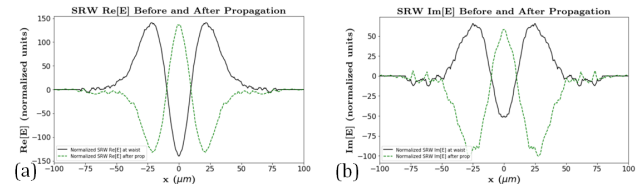
Figure 8: Horizontal electric field at waist and after SRW propagation through FELO beamline. a) Re[E] b) Im[E].

(a) (b) (c)
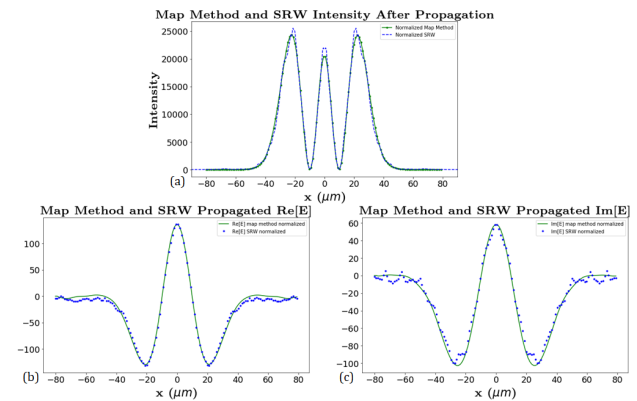
Figure 9: Comparison of SRW and map method propagation results for a) intensity, b) Re[E], and c) Im[E].

Timing Comparison Between SRW and Map Method Calculations

As with the moment calculations, the aforementioned calculations were all performed on the Radiasoft Jupyter server. The initial wavefront is computed in the same

way for both methods and took several seconds for the grid size used. The propagation through the FELO beamline in SRW took 43 seconds and was approximately the same for both Gaussian and non-Gaussian wavefronts. As with the moment calculations, SRW propagation parameters were tuned to achieve adequate results. We tried to ensure good resolution on the resulting electric fields while minimizing the overall grid sizes.

The calculation of the Wigner function and propagation for the method took 38 seconds and was approximately the same for both Gaussian and non-Gaussian wavefronts. As can be seen, the algorithms as implemented are comparable in speed. A large amount of the time for the map method came from the deposition of the transformed Wigner function. A more efficient algorithm for that process is conceivable. In addition we note that for a longer and more complex beamline, the SRW calculation would increase in time whereas the map method would not, once the transfer matrix has been computed.

CONCLUSION

We have demonstrated the use of a map based method for radiation transport through a beamline. We applied this method to a simple 4 crystal recirculation beamline which may be used for a free electron laser oscillator. For Gaussian wavefronts, only moment transport is required. We showed that such moment transport using a transport matrix for the beamline agrees very well with a more complete wavefront computation using the SRW code. The moment transport is substantially faster, by a factor of 608 for this particular case. In order to apply the method to non-Gaussian wavefronts, we computed the numerical Wigner function from the wavefront and demonstrated the linear transformation in phase space of this Wigner function. We did this both for a Gaussian and for an $m_x = 2$ Hermite Gaussian mode. We then reconstructed the electric field and showed good agreement with SRW simulation. We considered cases in which the field profile is separable so that we could work with 2-D phase space instead of 4-D phase space. In this case, the map method was found to be comparable in speed with the SRW calculation. However, as discussed, we expect that we may be able to speed up the map calculation, and in addition it would be substantially faster in the case of a beamline containing a larger number of optical elements. Regardless of the complexity, transport of the wavefront through the beamline is all contained within a single transfer matrix. Finally, we point out that partial coherence may be included in the Wigner function and the transport of this Wigner function is no more complicated than the case of a fully coherent beam.

Next steps include development of the corresponding routines for 4-D phase space, computation of the transfer matrix for arbitrary beamlines using a ray tracing code such as SHADOW, inclusion of partial coherence in the Wigner function, treatment of polarization, and inclusion of elements such as apertures or elements where the linear transport is not applicable and require special direct transformation of the Wigner function. In this latter case, we envisage using matrices for partial maps between such elements, and still expect a substantial speed up over the full wavefront propagation.

For the FELO simulations, we expect to be able to combine these simulations with a rapid FEL model to allow us to model the build-up of coherence within a manageable computation.

ACKNOWLEDGEMENTS

REFERENCES

[1] M. Sanchez del Rio, N. Canestrari, F. Jiang, and F. Cerrina, "SHADOW3: a new version of the synchrotron X-ray optics modelling package", *Journal of Synchrotron Radiation*, vol. 18, no. 5, pp. 708–716, 2011. `doi:10.1107/S0909049511026306`

[2] O. Chubar and P. Elleaume, "Accurate and Efficient Computation of Synchrotron Radiation in the Near Field Region", in *Proc. EPAC'98*, Stockholm, Sweden, paper THP01G, pp. 1177-1179, Jun 1998.

[3] K.-J. Kim, "A new formulation of synchrotron radiation optics using the Wigner distribution", LBL-20630, Berkeley, CA, USA, Nov 1985.

[4] K.-J. Kim and Y. V. Shvyd'ko, "Tunable optical cavity for an x-ray free-electron-laser oscillator", *Phys. Rev. Special Topics - Accelerators and Beams*, vol. 12, pp. 030703, 2009. `doi:10.1103/PhysRevSTAB.12.030703`

[5] T. Curtwright *et al.*, "Features of time-independent Wigner functions", 1997. `arXiv:hep-th/9711183`

[6] I. V. Bazarov, "Synchrotron radiation representation in phase space", 2011. `arXiv:1112.4047`

[7] A. Siegman, *Lasers*, University Science Books, Palo Alto, CA, 1986.

[8] `https://jupyter.radiasoft.org`